UC Santa Cruz

UC Santa Cruz Previously Published Works

Title

Isospectral intermediates in the photochemical reaction cycle of anion channelrhodopsin GtACR1.

Permalink

https://escholarship.org/uc/item/60n5c9hx

Journal

Biophysical Journal, 122(20)

Authors

Schleissner, Pamela

Szundi, Istvan

Chen, Eefei

et al.

Publication Date

2023-10-17

DOI

10.1016/j.bpj.2023.09.009

Peer reviewed

Isospectral intermediates in the photochemical reaction cycle of anion channelrhodopsin *Gt*ACR1

Pamela Schleissner,[1] Istvan Szundi,[1] Eefei Chen,[1] Hai Li,[2] John L. Spudich,[2] and David S. Kliger[1,*]

[1]Department of Chemistry & Biochemistry, University of California Santa Cruz, Santa Cruz, California and [2]Center for Membrane Biology, Department of Biochemistry & Molecular Biology, University of Texas Health Science Center at Houston McGovern Medical School, Houston, Texas

ABSTRACT   The most effective tested optogenetic tools available for neuronal silencing are the light-gated anion channel proteins found in the cryptophyte alga *Guillardia theta* (*Gt*ACRs). Molecular mechanisms of *Gt*ACRs, including the photointermediates responsible for the open channel state, are of great interest for understanding their exceptional conductance. In this study, the photoreactions of *Gt*ACR1 and its D234N, A75E, and S97E mutants were investigated using multichannel time-resolved absorption spectroscopy. For each of the proteins, the analysis showed two early microsecond transitions between K-like and L-like forms and two late millisecond recovery steps. Spectral forms associated with potential molecular intermediates of the proteins were derived and their evolutions in time were analyzed. The results indicate the presence of isospectral intermediates in the photocycles and expand the range of potential intermediates responsible for the open channel state.

SIGNIFICANCE   Channelrhodopsins are the most effective optogenetic tools available for neuronal silencing. Mechanistic information on channel opening of *Gt*ACR1 is particularly important since knowledge about their function could lead to more efficient channels. Although photoreactions of *Gt*ACR1 have been studied before, most of those studies have probed the wild-type protein and used single-wavelength monitoring of spectral changes. Here, photoreaction kinetics of *Gt*ACR1 and its D234N, A75E, and S97E mutants were investigated using multichannel time-resolved absorption spectroscopy. These results have yielded more detailed information showing that there are multiple isospectral forms involved in the channel-opening photocycle and that the nature of the channel-opening intermediates must be different from that suggested previously.

INTRODUCTION

Channelrhodopsins have received a considerable amount of attention in recent years as they provide a means to control neurons with light using a technique called optogenetics. The two anion channelrhodopsins (ACRs) from *Guillardia theta* were discovered in 2015 through a Basic Local Alignment Search Tool of the cryptophyte alga's genome (1). ACRs from *G. theta* (*Gt*ACRs) have been shown to inhibit activity and control behavior in a wide range of living animals (2–6). *Gt*ACR1 is particularly advantageous for optogenetic application as it was found to have higher unitary conductance than all other channelrhodopsins that were so far discovered, with the recently reported exception of kalium channelrhodopsins (7).

The photochemical reaction mechanism is important for understanding the high conductance of *Gt*ACR1, identifying the photointermediates responsible for the open channel state, and understanding how they regulate the channel current. For microbial rhodopsins, including *Gt*ACR1, the frequently used conventional naming system of the photocycle, K, L, M, N, O, is identical to the nomenclature used for the well-known proton pump bacteriorhodopsin (BR). K is a red-shifted, early intermediate, and L, M, and N are all blue-shifted intermediates, with M being the most blue-shifted one associated with the deprotonated Schiff base-linked retinal. For BR, this deprotonation is coupled to a proton being translocated across the membrane (8). O is a red-shifted late intermediate.

Electrophysiological and single-wavelength spectroscopic studies observed the M intermediate appearing after the onset of the current and ruled out the possibility of the M intermediate being the conductive state (9). The formation of the blue-shifted M form correlates with the fast decay

of the current, suggesting the deprotonation of the Schiff base is related to the closing of the channel. The depletion of M was temporally proximal to the slow decay of the current. This contrasts with the cation channelrhodopsin, ChR2, where the retinal Schiff base deprotonates before the channel opens and also BR where the deprotonation is directly involved with proton translocation (10).

Single-wavelength kinetic spectroscopic studies reported transitions from K to L at ~1 μs and ~20 μs. These were the only transitions found before the current rise times, and the L-state was proposed to be the open-channel intermediate of *Gt*ACR1 (9). Time-resolved Fourier-transform infrared spectroscopy studies identified an additional transition based on spectroscopic bands associated with backbone amide conformational changes (11). This new transition, with a lifetime of ~2 ms, was defined as L1/L1' to L2, with L1/L1' as early, nonconducting mixed states or possibly two consecutive states, and L2 defined as the conducting intermediate. The additional transition did not coincide with the major component of channel opening at 86 μs (12). A precise temporal correlation between the current onset and formation of a photointermediate is still lacking.

Here we report the kinetic results obtained from the analysis of time-resolved absorption difference spectra of wild-type (WT) *Gt*ACR1 and the D234N, A75E, and S97E mutants. Mutants D234N and S97E of low level of conductance are compared to the WT and the A75E mutant of normal conductance levels to gain information about the intermediate responsible for the open channel state. Using global kinetic analysis and spectral deconvolution, we derive the spectral forms that represent potential intermediates in the photoreactions and present a quantitative analysis of their evolution in time. Based on our results, we propose the presence of isospectral intermediates in the photoreactions and question the current view on *Gt*ACR1 photocycle kinetics, including the spectral nature of the intermediate responsible for channel opening.

MATERIALS AND METHODS

Expression and purification of WT *Gt*ACR1 and mutants

The gene for WT *Gt*ACR1 was purchased from Addgene (Watertown, MA) and ligated with a C-terminal 8×His tag between the *Hind*III and *Eco*RI restriction sites in a pNT79i vector kindly provided by Prof. Seth Rubin (University of California, Santa Cruz). *Spodoptera frugiperda* (Sf9) insect cells and ESF 921 cell culture medium were purchased from Expression Systems (Davis, CA). Cells were plated to a density of 2×10^6 cells/mL and transfected with TransIT-Insect Transfection Reagent (Mirus Bio, Madison, WI) in a TransIT-to-bacmid ratio of 2:1 (v/v). Suspension cells were grown to a density of 2×10^6 cells/mL and infected with P3 recombinant baculovirus at a virus-to-cell ratio of 1:20 (v/v). All-*trans*-retinal (Sigma-Aldrich, St. Louis, MO) in ethanol was added for a final concentration of 5 μM at the start of the infection. Cells were incubated at 27°C in a spinner flask at 240 rpm for 72 h. The S97E, D234N, and A75E mutants were grown from *Pichia pastoris* integrant cells. These cells were plated on yeast extract-peptone-dextrose with 2 mg/mL geneticin (G418), graciously donated by Prof. Douglas Kellogg (University of California, Santa Cruz),

for 3–4 days at 30°C. Single colonies were inoculated in a buffered glycerol-complex medium and grown until the optical density at 600 nm reached between 4 and 6. Buffered glycerol-complex medium was replaced with buffered methanol-complex medium, and expression was induced with the addition of 1% methanol. Cultures were supplemented with all-*trans*-retinal in methanol to a final concentration of 5 μM at the start of the expression and grown overnight (12–18 h) at 30°C while shaking at 240 rpm. Harvested Sf9 and *P. pastoris* cells were pelleted in a Fiberlite F9-6 rotor at 4000 rpm and stored at −80°C until purification.

Cells were resuspended in lysis buffer containing 20 mM 4-(2-hydroxyethyl)-1-piperazineethanesulfonic acid (HEPES) at a pH of 7.4, 300 mM sodium chloride (NaCl), 5% glycerol, 0.1 mM phenylmethylsulfonyl fluoride (PMSF), and 1 mM ethylenediaminetetraacetic acid (EDTA). Sf9 insect cells were lysed using sonication at a frequency of 20 MHz, 10 s on and 40 s off for six cycles on ice at 4°C. *P. pastoris* cells were lysed using a French press with a pressure of ~15,000 psi and the cell press cooled to 4°C. All subsequent purification steps were identical for the two cell types. Lysed cells were centrifuged at 4°C at a speed of $4500 \times g$ for 10 min in an Eppendorf 5810R centrifuge and then at a speed of $151,000 \times g$, in a 70Ti rotor, for 1 h in a Beckman Optima L-90K ultracentrifuge. The supernatant was discarded. The pellet was resuspended in 20 mM HEPES pH 7.4, 300 mM NaCl, 5% glycerol, 0.1 mM PMSF, and 1 mM EDTA, and homogenized with a glass Dounce homogenizer, ~20 strokes, on ice. The homogenous mixture was then supplemented with 1% n-dodecyl-β-D-maltoside (DDM; Anatrace, Maumee, OH) and solubilized anywhere from 1 h to overnight at 4°C while nutating. The solubilized solution was centrifuged at $151,000 \times g$ for 1 h. Depending on the yield, the pellet process was repeated where the pellet from the second ultracentrifuge step was subsequently resuspended, homogenized, and solubilized with a total of 2% DDM for 1 h to overnight. This process was never repeated for a third time and the total DDM concentration for solubilization did not exceed 2%. The supernatant was incubated with nickel-nitrilotriacetic acid (Ni-NTA) agarose beads (Thermo Fisher Scientific) for 1 h. Ni-NTA resin was equilibrated with 20 mM HEPES pH 7.4, 300 mM NaCl, 5% glycerol, 0.1 mM PMSF, 1 mM EDTA, and 0.03% DDM. The Ni-NTA resin was step-wise washed with the equilibration buffer supplemented with 20 mM and 40 mM imidazole. Each step was 20 column volumes. The protein was eluted with the same buffer supplemented with 400 mM imidazole. Buffer exchange and concentrating the protein were performed with a 30 kDa MWCO filter. For the buffer exchange, the protein was flushed with the appropriate buffer at least three times. Proteins were concentrated to at least 1 mg/mL, flash frozen in liquid nitrogen, and stored at −80°C for future experiments.

Time-resolved optical absorption measurements

Time-resolved optical absorption experiments of *Gt*ACR1 and mutants were performed using 532-nm pulsed laser light (~7-ns full width at half maximum, 0.5 m J/mm^2) from a Quanta Ray Q-switched DCR-11 neodymium-doped yttrium aluminum garnet laser (Spectra Physics, Milpitas, CA) to excite the sample. Probe pulses were produced with a xenon flash lamp. Spectra were detected with an *i*Star ICCD detector (model no. DH720-25F-03, Andor Technology, Belfast, Northern Ireland) coupled to the pump-probe system via a delay generator (model DG535 Stanford Research Systems, Sunnyvale, CA) (13). For WT, D234N, and S97E, measurements were recorded at 22 delay times, logarithmically spaced between 100 ns and 1 s. The A75E mutant was measured at 23 logarithmically spaced delay times between 100 ns and 2s. At each delay time, a minimum of 100 averages were recorded. All time-resolved optical absorption experiments were performed at room temperature using a 0.4-cm pathlength quartz cuvette with a plastic insert that resulted in a 10-μL observation chamber. Fresh sample was injected in 10-μL aliquots into the cuvette before each photoexcitation to prevent any secondary photoreactions.

The reproducibility of the spectral data was tested on the WT protein sample at pH 7.4. Individual protein samples were produced independently in two laboratories and spectral data were collected on each sample on two different days. Comparison of the normalized spectral data showed good

agreement between the individual datasets. Records taken on two different days on the same sample were averaged. The data presented for the mutants, and the WT at other pH values, are averages of spectral records taken on a single protein sample.

Data analysis

Time-resolved optical absorption difference spectra were analyzed with programs written in MATLAB (MathWorks) following protocols described in (14). Briefly, data analysis assumed all transitions followed first-order kinetics and the concentrations of the intermediates can be described by time-dependent exponential functions. The time dependence of the optical absorption difference spectra, the difference between post- and pre-illumination, was fitted with a series of exponential functions, $\Delta A(\lambda, t) = \sum_n b_n(\lambda) \exp(-r_n t) + b_\circ(\lambda)$, where t is time, λ is wavelength, r_n are the apparent rates, and $b_n(\lambda)$, the amplitudes of the exponentials, are the b-spectra. The dataset was subjected to singular value decomposition (SVD), a process that separates the temporal and spectral components of the time-resolved difference absorption spectra, $\Delta A = \mathbf{U}\mathbf{S}\mathbf{V}^{\mathbf{T}}$ (15). The entire dataset can be approximated by a limited number of the significant orthonormal spectral vectors, $\mathbf{U}$, and temporal vectors, $\mathbf{V}$. Global exponential fitting of the significant temporal vectors produced the apparent rates, r_n. The b-spectra, $b_n(\lambda)$, were determined from the spectral vectors, $\mathbf{U}$, the significance values, $\mathbf{S}$, and the results of the V-vector fit. The b-spectra carry all the information about spectral changes at each apparent lifetime and can be interpreted in terms of a chemical reaction (16). The b-spectra were converted into spectra of the straight sequential scheme. The intermediate spectra of the sequential scheme may or may not represent single molecular states. In most cases, they are mixtures of states co-existing in a particular time window. In the analytical process used in this work, the sequential intermediates, $\mathbf{In}(\lambda, n)$, were deconvoluted into spectral forms, $\mathbf{In}(\lambda, n) = \mathbf{E}(\lambda, m) \times \mathbf{Q}(m, n)$, where $\mathbf{E}(\lambda, m)$ is the matrix of the spectral forms and $\mathbf{Q}(m, n)$ is the composition matrix showing the amount of each spectral form, m, contained within each intermediate spectrum, n. Here, spectral form refers to an absorption spectrum that characterizes the state of the chromophore, as opposed to an intermediate spectrum, which is the spectrum of a member of a proposed kinetic scheme. Each spectral form may represent a single intermediate or multiple intermediates of the unknown reaction mechanism. In the latter case, the intermediates are called isospectral. The time evolution of the spectral forms were then calculated as a product of the composition matrix, $\mathbf{Q}(m,n)$, and the time-dependent concentration of the sequential intermediates, $\mathbf{C_{in}}(n, t)$.

RESULTS AND DISCUSSION

Time-resolved absorption difference spectra, post minus pre-photoexcitation, of *Gt*ACR1 were recorded between 350 and 725 nm. The results are shown in Fig. 1 for the WT (Fig. 1 *A*) and the mutants D234N (Fig. 1 *B*), A75E (Fig. 1 *C*), and S97E (Fig. 1 *D*), all at pH 7.4. The spectra were recorded at 22 logarithmically spaced delay times from 100 ns to 1 s after laser excitation for both the WT and the mutants, except the A75E mutant, which had an additional 2-s delay time recorded. The arrows represent the direction of spectral changes in the different spectral regions and the left arrow of the double arrows indicates changes at times earlier than those for the right arrow. The evolution of spectra suggests similar early-time kinetics but significant differences in the kinetics between these proteins at later times.

To get more insight, the spectral data were analyzed by SVD. Because there are only a limited number of intermediates involved in a reaction cycle, the entire dataset is a linear combination of a limited number of spectral forms. SVD decomposes the data matrix into the product of three matrices that contain the orthonormal spectral vectors, $\mathbf{U}$, the orthonormal temporal vectors, $\mathbf{V}$, and a diagonal matrix, $\mathbf{S}$, which shows the relative contributions by the $\mathbf{U}$ and $\mathbf{V}$ vector pairs to the data. In the ideal case of noiseless data, the number of nonzero $\mathbf{U}$ and $\mathbf{V}$ vector pairs gives the number of intermediates in the underlying reaction. With real experimental data, this is more complex. Because of experimental noise, there are no $\mathbf{U}$ and $\mathbf{V}$ vectors of zero amplitude, only vector pairs having amplitudes of diminishing significance. Furthermore, if two or more of the intermediates have the same spectra within experimental spectral resolution (i.e., are isospectral), the number of independent spectral shapes, and thus the number of significant $\mathbf{U}$ vectors, that constitutes the dataset is less than the number of intermediates involved in the reaction. Despite these drawbacks, analysis of the contributions to the dataset by the $\mathbf{U}$ and $\mathbf{V}$ vector pairs can give valuable information. The contributions to the recorded spectral data by the $\mathbf{U_i}$ and $\mathbf{V_i}$ vector pairs, $\mathbf{U_i}\mathbf{S_i}\mathbf{V_i}^{\mathbf{T}}$, with decreasing significance are shown in Fig. 2 *A–D* for the WT, D234N, A75E, and S97E mutants at pH 7.4, respectively. For each protein, the contribution of pair(3) is multiplied by 5, and that of pair(4) and the less significant ones are multiplied by 10 for easier comparison. For the WT in Fig. 2 *A*, the contributions of pairs(1,2,3) are clearly significant, whereas that of pair(4) is hardly above the noise level. Pair(5) is at the level of the noise vector pair(11). Thus, the dataset can be reproduced by four vector pairs, which means there are no more than four independent spectral forms in the photoreaction. For the D234N mutant the contributions of pairs(1,2,3) are significant, whereas pair(4) contributes very little. The A75E mutant is very similar to the WT, showing clearly significant contributions by pairs(1,2,3), and that by pair(4) only slightly above the noise level. The same is true for the S97E mutant. Thus the number of significant vector pairs, and thus the number of independent spectral forms in the photoreactions of the mutants, do not exceed four either.

Global exponential fitting

After selecting the significant $\mathbf{U}$, $\mathbf{V}$ vector pairs, the $\mathbf{V}$ vectors were fitted with sums of exponential functions. The number of exponential functions necessary for adequate fit is determined by judging the residuals, the difference between the experimental and fitted $\mathbf{V}$ vectors weighted by their significance values, $\mathbf{Vmisfit} = \mathbf{S} * (\mathbf{Vexp} - \mathbf{Vfit})$. The amplitudes and shapes of the $\mathbf{V}$-vector misfits were compared to the $\mathbf{V}$ vectors of low significance that are considered to represent noise only. The misfits were also tested for nonrandomness using the autocorrelation function for discrete vectors in
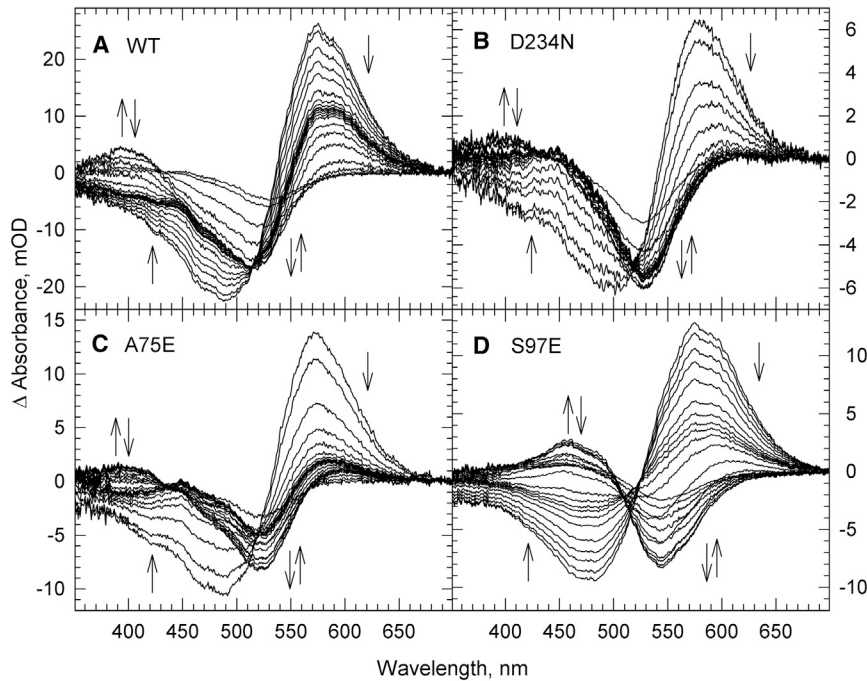
FIGURE 1 Time-resolved absorption data. Post-minus pre-excitation data of (*A*) WT *Gt*ACR1 along with the (*B*) D234N, (*C*) A75E, and (*D*) S97E mutants at pH 7.4. SVD filtered for clarity. For the double arrows, the left one represents times earlier than the right arrow.

which the product of **V**misfit(1:n − 1) and **V**misfit(2:n) is normalized (lag 1). Positive autocorrelation coefficients above ∼0.1 are indications of significant nonrandomness. Fig. 3 shows the misfits for the WT, D234N, A75E, and S97E mutants at pH 7.4 in panels Fig. 3 *A–D*, respectively. For all samples, three exponentials are not sufficient to

adequately fit the data, as the residuals are way above the level of noise vectors and clearly show nonrandom wave-like structures stretching over two decades of time. The auto-correlation coefficients for the misfits of the WT, D234N, A75E, and S97E mutants were in the range of 0.5–0.7, 0.5–0.7, 0.4–0.7, and 0.1–0.6, respectively. Such structures and
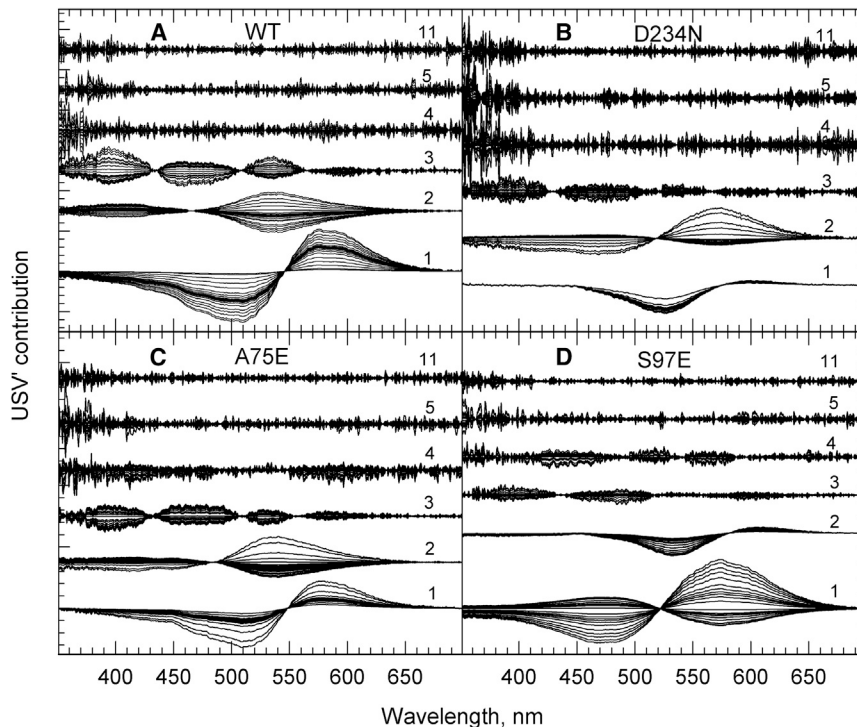

FIGURE 2 Contributions by **U** and **V** pairs from SVD to the spectral data. (*A*) WT GtACR1, (*B*) D234N, (*C*) A75E, and (*D*) S97E mutants at pH 7.4. Numbers correspond to the **U** and **V** pairs in order of their significance.
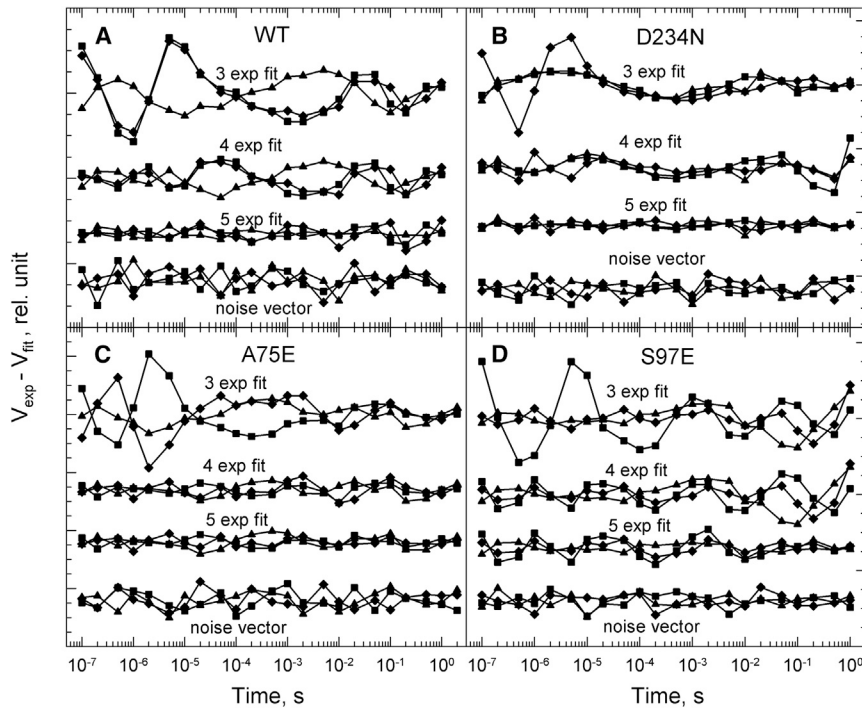
FIGURE 3 Difference between experimental and fitted **V** vectors for three, four, and five exponential fits. (*A*) WT GtACR1, (*B*) D234N, (*C*) A75E, and (*D*) S97E mutants at pH 7.4. The misfits of **V1** (square), **V2** (diamond), and **V3** (triangle) are compared to vectors 11, 12, and 13, which represent noise.

positive autocorrelation coefficients indicate the need for additional exponentials. The biggest misfits are in the microsecond region, which is reduced by adding one more exponential to the fit yielding two well-separated lifetimes, one in the submicrosecond and one in the microsecond region. In the four-exponential fit, the WT and the D234N mutant still show nonrandom, wave-like misfits in the late-microsecond to early-millisecond time window, whereas the S97E mutant has big misfits in the late-millisecond range. They showed autocorrelation coefficients in the range of 0.38–0.6 for the WT, 0.13–0.28 for two **V** vectors of D234N, and 0.1–0.6 for two **V** vectors of S97E. The misfits for the A75E mutant are seemingly more random. However, all show 0.1–0.4 positive autocorrelation coefficients. The nonrandom misfits become further randomized in the five-exponential fit and most of the autocorrelation coefficients drop to zero or below, indicating that there is no need for more exponentials in the fit. Note that fitting more exponentials not only randomizes the misfits but also reduces their amplitudes. However, once the nonrandom, wavy structure is removed from the misfits, adding more exponentials for the sake of amplitude reduction has no justification. Thus, using six-exponential fits is not justified despite the significant reduction of the misfit amplitudes (not shown). The analysis presented here will be based on the five exponential fits for all the proteins. The conclusions of this work can be reached even if the data are underfitted by using the four-exponential fit, as discussed below for the A75E mutant. For a detailed kinetic analysis in the future, however, the information provided by the five-exponential fit may be necessary.

In the algebraic analysis method we use, the experimental errors in the spectral data matrix propagate into errors of lifetimes or apparent rates via the **V** vectors, and into errors of b-spectra via both the **U** and **V** vectors, derived in SVD. The desire to calculate these errors and, perhaps, interpreting the errors of the apparent rates as errors of reaction rate constants faces two obstacles. First, the apparent rates do not come from a linear fit, which is relatively easy to handle. Whether or not SVD is used in the fit, the apparent rates are the result of nonlinear fit, and calculation of their errors poses a significant mathematical challenge. Second, contrary to the general conception, the exponential fit is not connected to any particular scheme. The apparent rates from the exponential fit do not a priori represent reaction rate constants in a sequential scheme, as is sometimes falsely interpreted. Rather, the lifetimes and b-spectra are merely mathematical abstractions, as is the exponential fit itself, and gain physical meaning only when applied to a mechanistic scheme that is often more complex than the sequential scheme (13,14,16). Because it is very difficult to connect the errors of the apparent rates to the errors of the microscopic rate constants in a complex scheme, knowing the errors of the apparent rates would be of little use. Instead of attempting to calculate errors of the fit, we find it far more practical and useful to make estimates based on the range of values found in repeated experiments and evaluate the influence of their uncertainties on the conclusions drawn.

The apparent lifetimes, the inverse of apparent rates, from the five-exponential fit are 0.49 μs, 5.2 μs, 0.76 ms, 22 ms,

and 0.17 s for the WT; 0.30 μs, 2.3 μs, 360 μs, 28 ms, and 1 s for D234N; 0.37 μs, 4.8 μs, 2.6 ms, 15 ms, and 0.85 s for A75E; and 0.62 μs, 5.6 μs, 0.69 ms, 57 ms, and 0.45 s for S97E mutant. Fig. 4 shows the amplitude spectra, called b-spectra, bs1–bs5, corresponding to the five lifetimes, and also the spectrum of the final product, b0, in the experimental time window. The few lifetimes, reported only for the WT, from single-wavelength measurements (9,11), agree reasonably well with our results, except the lifetimes shorter than a few microseconds, which are too fast for accurate detection in single-wavelength experiments. Repeated experiments done on the WT protein gave the following ranges for the five lifetimes listed: 0.3–0.6 μs, 4–6 μs, 0.2–2 ms, 20–26 ms, and 0.15–0.22 s, respectively. The range of uncertainties presented here for the individual records of varying amplitudes becomes narrower when two or more records are averaged together. The lifetimes listed for the WT above represent the average of three experiments. For the WT, the third lifetime shows the biggest uncertainty because it belongs to a small-amplitude b-spectrum, as seen in Fig. 4 A. The general rule is that the smaller the amplitude of the b-spectrum, the wider is the range of uncertainty in the value of the corresponding lifetime. Because the contributions by small-amplitude b-spectra to the data are also small, in most cases, they have little influence on the conclusions drawn.

The sub-microsecond lifetime in all experiments has bigger uncertainty than the microsecond lifetime because it is based on smaller number of recorded spectra (the first delay time is 100 ns). The same applies to the longest lifetime for all the mutants, especially for the 1-s lifetime of the D234N mutant. The uncertainties of the longest lifetimes cause some uncertainties in the amplitudes of the late-millisecond and b0 spectra, which do not affect our conclusions.

There is a common pattern seen in the lifetimes: there are two early-microsecond and two late-millisecond transitions for all the proteins. This gives assurance that the exponential fit captured a common kinetic trend the GtACR1 proteins follow. The two early-microsecond b-spectra, bs1 and bs2, for the WT, the D234N, and the S97E are very similar, whereas those for the A75E mutant differ in amplitude. All are consistent with the decay of a red-absorbing form into a blue-absorbing one, such as the K to L transition in BR but occurring in two steps. This fast two-step transition has not been resolved satisfactorily in single-wavelength experiments before. The third and fourth b-spectra show more variations between the proteins, indicating larger differences in the kinetics in the early- and late-millisecond time windows. Only the fifth b-spectra, which correspond to the recovery process that leads to the products in the b0 spectra, have similar shapes. The b0 spectra have nonzero amplitudes, suggesting slow spectral changes occurring on the minute timescale, which is in agreement with data in reference (9). Thus, the recorded kinetics ends not in complete recovery of the dark (unphotolyzed) state (12) but at an earlier stage we call the recovered state. The same phenomenon has been seen in cation channelrhodopsin kinetics (13).

A comparison between the results of the SVD analysis presented above and those of the global exponential fit leads to an important conclusion. SVD showed no more than four
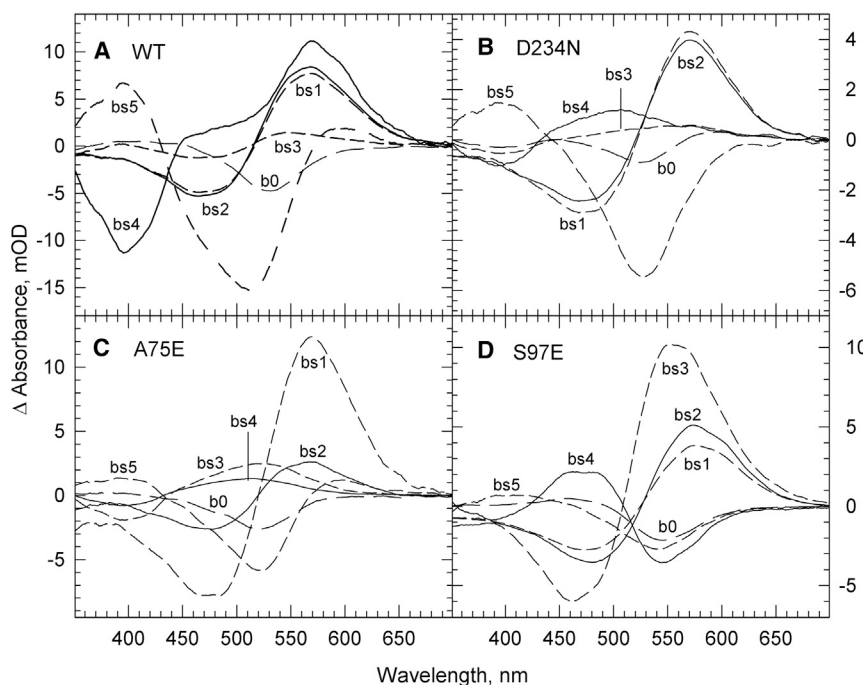

FIGURE 4 Spectral changes, b-spectra, for the apparent lifetimes produced by the five-exponential fit. (A) WT, (B) D234N, (C) A75E, and (D) S97E **V** vectors. The spectra are smoothed for clarity.

spectral forms being present in the absorption data matrix. The kinetic matrix of four intermediates, however, produces only three nonzero apparent rates and not more. The need for more than three exponentials for adequate fit clearly indicates that there are more than four, most likely six, intermediates in the photocycle, and thus several intermediates must have the same spectra. In other words there must be a number of isospectral intermediates involved in the reaction. Deriving and testing kinetic models is a complex task (13,14,16) that goes beyond the scope of this study. Thus we have no intention to derive, propose, or even test any reaction scheme for *Gt*ACR1 in this work. Without assuming a scheme, we can, however, identify the spectral forms that constitute the spectral data matrix, as we have done in previous reports (13,14). These spectral forms can serve as absorption spectra of intermediates in future kinetic models. Analyzing the time evolution of these forms can give important clues for future kinetic studies and can help identify the spectral form associated with the channel open state.

Derivation of spectral forms

The term spectral form refers to an absorption spectrum characteristic of the state of the chromophore. It may belong to a single intermediate or multiple ones if the photocycle has isospectral intermediates. The SVD results above predicted no more than four spectral forms in the spectral data, which, according to the results of the exponential fit, are shared by more than four, possibly six or more, unknown intermediates. The orthogonal **U** vectors and the b-spectra

from the exponential fit have both positive and negative spectral contributions from the intermediates and thus they are not the optimal source to deduce the spectral forms. Note that the sum of exponentials obtained in the exponential fit can be interpreted as simultaneous, parallel decays of the b-spectra, each with its own apparent rate, stretching over the entire time window. There is no chemical reaction that follows this kind of a path. However, if the apparent rates are arranged not in a parallel but in a sequential way, it can be associated with a reaction chain that follows a sequential scheme. We use this sequential arrangement, and call it the straight sequential scheme, not as a potential mechanism of the photocycle but simply as a mathematical tool that allows us to derive the spectral forms in a relatively easy way. The sequential spectra calculated from the b-spectra, also called spectra of the sequential intermediates, have only positive contributions by the real intermediates of the unknown mechanism and thus they better suit our purpose (16). Interestingly, although the lifetimes obtained for the individual records may vary by a factor of 1.5, the sequential spectra are very similar and show amplitude variations rarely exceeding 5%. This is because small inaccuracies in the shapes of the individual spectra recorded at successive delay times have greater influence on the timing of the spectral change than on its amplitude.

Fig. 5 shows the difference spectra of the sequential intermediates, In1–In6, calculated from the b-spectra in Fig. 4. For technical reasons explained below, the difference spectra are not as convenient to deconvolute into spectral forms as are the absolute spectra, which can be constructed by adding appropriately sized spectra of the dark forms to
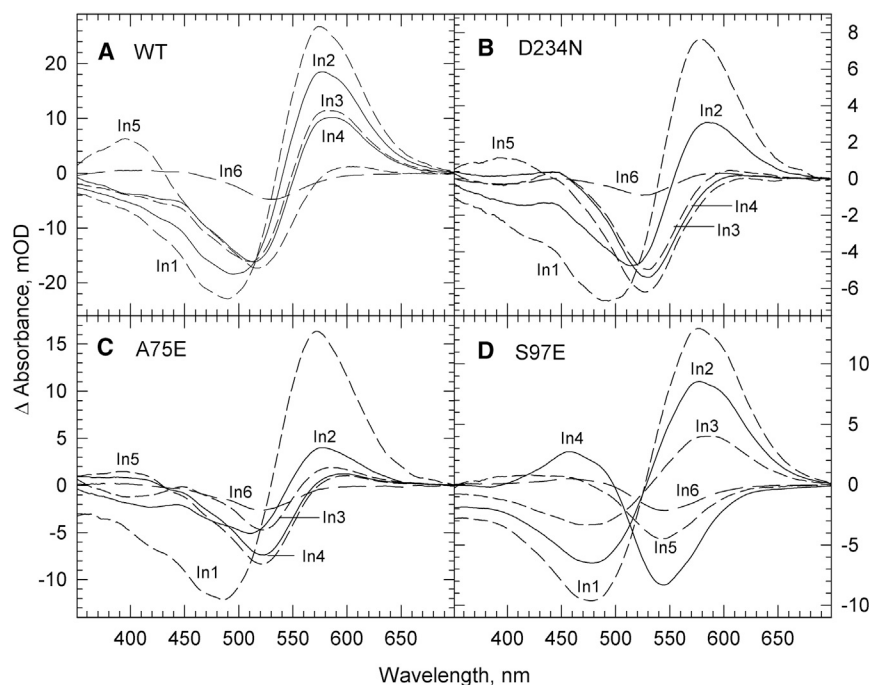

FIGURE 5 Intermediate difference spectra. (*A*) WT, (*B*) D234N, (*C*) A75E, and (*D*) S97E assuming a unidirectional sequential scheme. The spectra are smoothed for clarity.

the difference spectra. The amplitude of the added dark spectrum is deduced following a general rule of thumb we call the rule of similar spectral shapes (13). Briefly, intermediate spectra of retinal proteins, when plotted on the energy (wavenumber) scale and overlaid by shifting one of them, display similar shapes. Fig. 6 demonstrates the use of the rule and the construction of absolute (abs) intermediate spectra of sequential intermediates for the WT protein. Fig. 6 A shows In1 abs (solid) created by adding 50 mOD of the dark spectrum (solid) to In1 of Fig. 5 A. This amount was found to be suitable, as In1 abs closely overlays the energy-shifted dark-form spectrum (dashed lines). Note that we split the absorption spectrum into two bands, the main band in the visible region, the result of the so-called opsin shift, and a band in the UV region (350–400 nm), as displayed by the different dashed black lines. Only the environment-sensitive main band is shifted on the energy scale. The results of the dark-form addition to the sequential intermediates, defined as the absolute spectra, are shown in Fig. 6 B.

The procedure described for the WT was also applied to the other proteins. For all the proteins the first (In1) and last (In6) spectra are regarded as spectral forms of individual molecular states because they overlaid the dark-form spectra when shifted on an energy scale. We refer to In1 as K-like

and to In6 as recovered spectral form, R. The spectra In2–In5 in Fig. 6 have shapes that suggest they comprise multiple spectral forms. Many of these spectra exhibit fractions of the red-absorbing K-like spectral form. In5, and some of In4, display spectral contributions around 400 nm, resembling the M intermediate of the BR photocycle, which very likely corresponds to the deprotonated form of the retinal chromophore and will be called the M-like spectral form. For the purpose of deconvolution, the spectrum of this form was constructed based on the absorption spectrum of In5 for the WT protein at pH 8.5.

In the deconvolution of the absolute spectra of the sequential intermediates, increasing fractions of the K-like and M-like spectral forms were subtracted from them until complete removal was achieved in the spectral regions corresponding to the subtracted forms. The advantage of working with absolute spectra, rather than with difference spectra, is that over-subtraction results in negative absorbance values, which are easily noticed. For the WT and the S97E mutant, In5 also contained a substantial amount of the recovered form. The amplitudes of the spectra remaining after the subtractions, SP, were normalized to fraction value one for each of the In2–In5 sequential intermediates using the formula

$$SP = (In - a*K - b*M - c*R)/(1 - a - b - c)$$

The deconvolution was considered valid if the resulting spectrum, SP, overlaid the dark spectrum shifted on the energy scale, as described above.

The results of the spectral deconvolution for the four proteins are shown in Fig. 7. Interestingly, for the WT, D234N, and A75E mutants, the remaining components in the four intermediates, In2–In5, all have practically the same spectral shape, amplitude, and λ_{max} position within the experimental spectral resolution. Because, in BR kinetics, K is followed by L, we name this blue-shifted form L-like. Only S97E shows two remaining components: a less-blue-shifted L′-like spectral form in In2 and In3 having λ_{max} very similar to that of the recovered form, and the "common" L-like spectral form in In4 and In5. The transition between these forms caused the unusually large spectral change in the millisecond region, best shown by bs3 in Fig. 4 D. SVD analysis predicted no more than four spectral forms in the spectral data and in the deconvolution of sequential spectra we found these forms. Note that the L′-like and the R of S97E have practically the same shape. These four, or five in case of the S97E mutant, spectral forms can serve as spectra of the intermediates in future kinetic schemes.

The fractions of each of the spectral forms contained in the sequential intermediates for the four proteins are listed in Table 1. In this deconvolution technique, a 0.02 difference in fractional value can be recognized, which sets the relative accuracy and the detection limit to this value. Based on the results of the deconvolution, we can make a few conclusions. For each of the WT, D234N, and A75E proteins, the L-like forms in In2–In5 have the same spectral
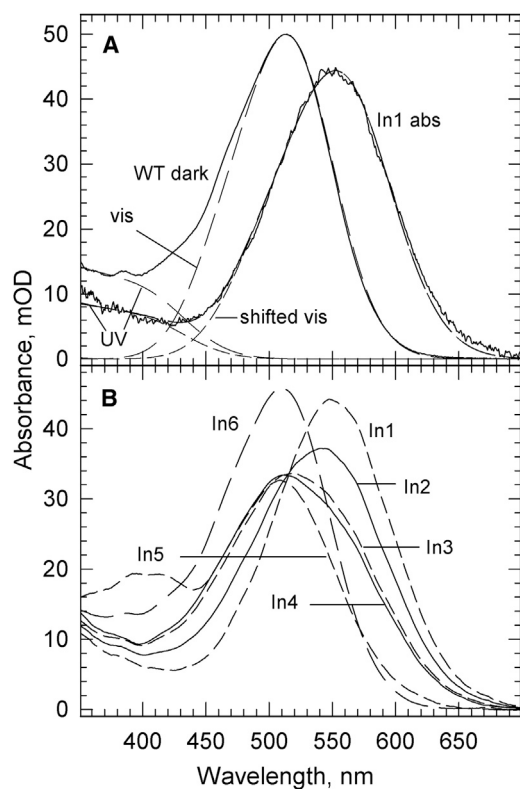

FIGURE 6 Absolute intermediate spectra. (A) In1 abs (solid) is formed by addition of the WT dark-form spectrum (solid) to In1 from the WT sequential intermediates in Fig. 5 A. The spectra are separated into visible and UV parts (dashed lines). In1 abs closely overlays the energy-shifted dark-form spectrum. (B) The results of the addition of dark-form spectrum to the sequential intermediates, referred to here as the absolute spectra.
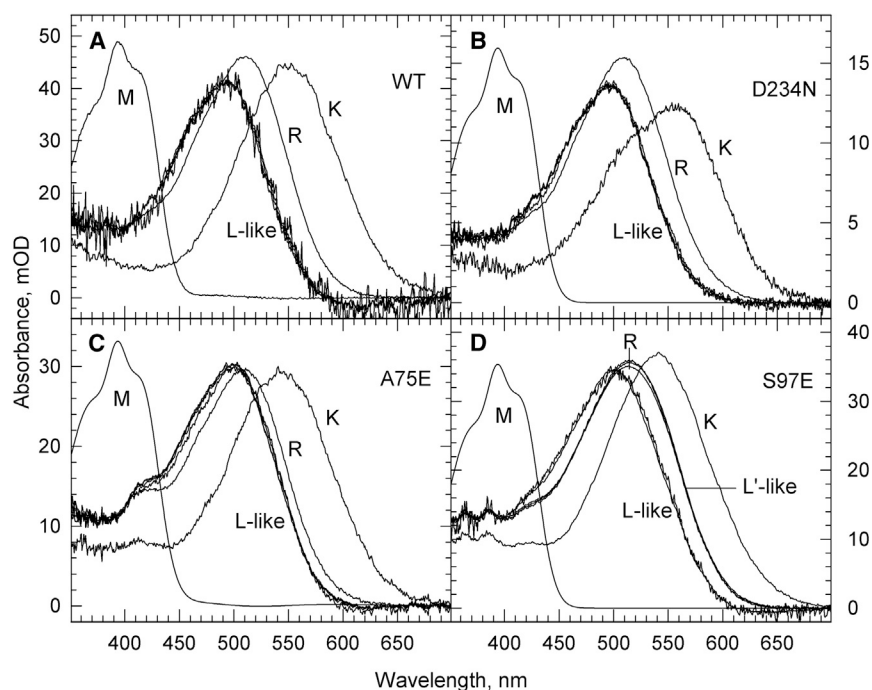
FIGURE 7 Spectral forms from the deconvolution of the sequential intermediates. (*A*) WT, (*B*) D234N, (*C*) A75E, and (*D*) S97E.

characteristics but occur at different times, suggesting that they represent isospectral intermediates in the unknown kinetic mechanism. Similarly, the K-like form present in In2–In5 does not necessarily have the same chemical environment or conformation as the K in In1 and thus may also represent isospectral intermediates. The fact that the sequential intermediates contain multiple spectral forms in a complex way strongly suggests that the sequential schemes proposed earlier (9,11) for describing the photocycle kinetics of *Gt*ACR1 may have serious shortcomings.

Time evolution of the spectral forms

The interpretation of the spectral changes in terms of sequential events, followed by extraction of the spectral forms, yielded the composition values in Table 1. The entries in the table represent the composition matrices, $\mathbf{Q}$, for the four proteins. The product of the composition matrix and the matrix of the time-dependent concentrations of sequential intermediates, $\mathbf{C}_{in}(n,t)$, gives the time evolution of the spectral forms $\mathbf{C}_{sp}(m,t) = \mathbf{Q}(m,n) * \mathbf{C}_{in}(n,t)$, where m is the number of spectral forms in the n intermediates and t is time. Note that $\mathbf{C}_{in}(n,t)$ is calculated using the eigenvalues and eigenvectors of the kinetic matrix for the sequential scheme (16) and thus can accommodate any timescale. For smoothness of the curves presented we use a log timescale having 10 points per decade. The concentration time dependence, the accuracy of the lifetimes from the exponential fit, is the major contributor to the uncertainty of the time-evolution curves. A factor of 1.5 inaccuracy in the lifetime of a dominant transition, estimated from the range of

lifetimes of the individual records, would shift the appropriate section of the curve back or forth along the time axis slightly. Also, a 10% inaccuracy of the fraction values would move the curves up or down somewhat. Neither of these would change the meaning of the time-evolution curves in any significant way; it will not affect the placement of the different spectral forms in the photocycle.

Fig. 8 *A* shows the relative concentrations of the spectral forms for the WT protein. The K-like and L-like spectral forms are present in the entire experimental time window, and starting from ~10 μs in similar amounts. Their evolution suggests an early equilibration between the two. The global exponential fit showed that the equilibration is a two-step process. The formation of the deprotonated M-like form coincides temporally not only with the decay of the L-like form, as reported (9), but also with the decay of the K-like form and with the partial formation of the recovered form. Patch-clamp electrophysiology studies (12) under single-turnover conditions report current onset at around 100 μs, which is presumably connected to a conformational change in this time region. Although both the K-like and L-like forms are present in large amounts, we did not observe any spectral transition at or near the time of current onset. The transition to the open-channel conformation appears to be spectrally silent, or to have spectral signature below our resolution, in the visible range but it is likely to have a signature in the infrared region (11) for WT *Gt*ACR1.

The time evolution of the spectral forms for D234N is shown in Fig. 8 *B*. The K-like and L-like forms for the D234N mutant appear to exist for the entire length of the experimental time window, similarly to the WT. The time

TABLE 1 Fraction composition of the sequential intermediates for WT, D234N, A75E, and S97E *Gt*ACR1

	In1	In2	In3	In4	In5	In6
WT						
K	1	0.76	0.56	0.51	0.14	–
L	–	0.24	0.44	0.49	0.20	–
M	–	–	–	–	0.20	–
R	–	–	–	–	0.46	1
D234N						
K	1	0.50	0.16	0.11	0.06	–
L	–	0.50	0.84	0.85	0.80	–
M	–	–	–	0.04	0.14	–
R	–	–	–	–	–	1
A75E						
K	1	0.38	0.25	0.21	0.19	–
L	–	0.62	0.75	0.70	0.69	–
M	–	–	–	0.09	0.12	–
R	–	–	–	–	–	1
S97E						
K	1	0.69	0.38	0.11	0.03	–
L'	–	0.31	0.62	–	–	–
L	–	–	–	0.89	0.24	–
M	–	–	–	–	0.03	–
R	–	–	–	–	0.70	1

Intermediates for WT, D234N, A75E, and S97E *Gt*ACR1.

evolution, together with the exponential fit, suggest an early equilibrium is established between K-like and L-like forms in two steps, similarly to the WT. However, after equilibration, much less of the K-like spectral form is present in this mutant compared to the WT. The M-like form appears earlier than in the WT and has a two-component rise, as reported (12), with the later rise coinciding with the decay of both the K-like and L-like forms. This suggests that not only the L-like but

also the K-like form may convert into the deprotonated M-like state. Starting from ~10 μs, the ratio of K-like to L-like form is much lower in the D234N mutant than in the WT. No spectral transition is observed at or near the time of current onset (17). Some studies on the D234N mutant have reported significant loss of function (6,18,19). A low-conducting variant of *Gt*ACR1 would disclose itself in the photoreaction as having the low level of the intermediate responsible for the open channel. As the L-like form is the major and the K-like form is the minor component in this mutant, it is more likely that the K-like form, and not the L-like form, is responsible for the conducting intermediate state.

Fig. 8 *C* shows the time-dependent changes of the spectral forms for the A75E mutant. Similarly to WT and D234N, the K-like and L-like spectral forms are present for the duration of the reaction and there is a two-step early equilibrium between the two spectral forms. In the submicrosecond transition, more K-like form decays in the A75E mutant than in the WT. There is little decay in the microsecond transition and thus, after the two decay steps, a significant amount of the red-absorbing K-like form is still present. Although the K-like to L-like ratio in the A75E is somewhat less than in the WT, it is much higher than in the D234N mutant. Again, no spectral transition matches the reported current onset (17). Because the four-exponential misfits shown above for this mutant were seemingly more random than for the other samples, we tested whether the number of exponentials chosen for the analysis plays a crucial role in our conclusions. The time dependences of the four spectral forms were calculated for the four-, five-, and six-exponential fits and compared. Their shapes agreed within 10%, indicating that the two
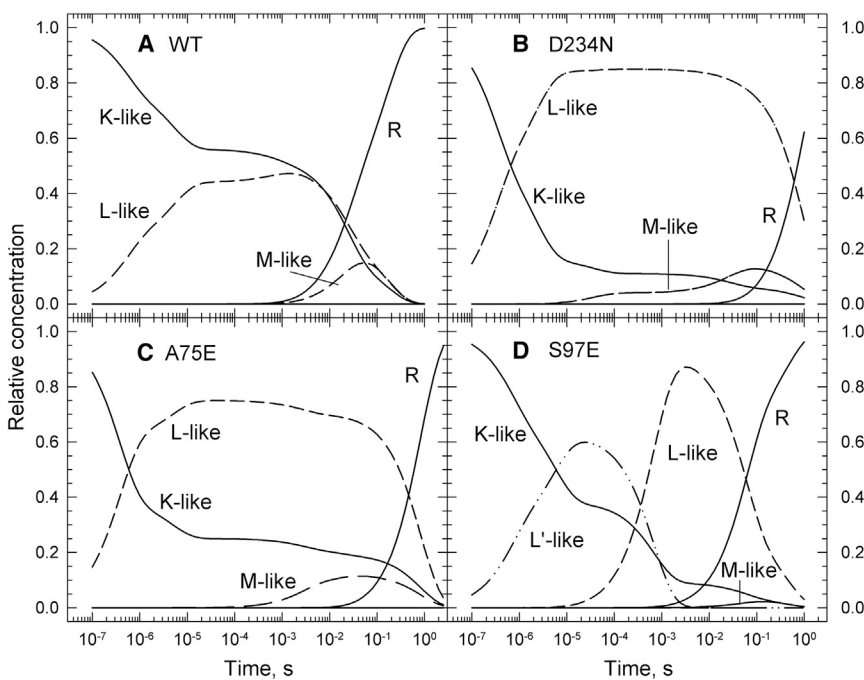

FIGURE 8 Time-dependent concentration profiles of the spectral forms. (*A*) WT, (*B*) D234N, (*C*) A75E, and (*D*) S97E at pH 7.4. A log timescale having 10 points per decade was used to produce the smooth curves.

early-microsecond and two late-millisecond lifetimes are the most important factors in shaping the time-evolution curves and comprise the basis for the conclusions drawn.

The time-dependent concentration profile of the S97E mutant is shown in Fig. 8 *D*. S97E revealed a distinct early spectral form, L′-like (Fig. 7 *D*), not seen in WT, D234N, and A75E. This form is much less blue shifted than the L-like forms in the WT and the other mutants. The K-like form decays to the L′-like spectral form in S97E the same way, in two steps, as it decays to the L-like form in the WT and the other mutants. The equilibrated mixture of the K-like and L′-like forms converts into the "normal" L-like form on the millisecond timescale. The presence of two, early and late, L-like forms, which are, luckily, spectrally different and thus easily detected, strongly supports our concept of multiple K-like and L-like intermediates being present in the photocycle. These are, presumably, structurally different but practically isospectral, and thus the transitions between them are spectrally silent in the visible region. One of these silent transitions may be correlated with the opening of the channel.

The S97E mutant showed significantly less current than the WT (9); thus, we would expect to see a small amount of the spectral form responsible for the open state in this mutant. The only spectral form that we observe in small amounts for S97E in the time window of the current is the K-like form.

pH dependence of the kinetics

In the published kinetic schemes (9,11), the M-like intermediate has an important role. It is involved in channel closure. To learn more about the spectral transitions under conditions that may influence Schiff base deprotonation, we also investigated WT *Gt*ACR1 at pH 5.5 and 8.5, D234N at pH 4.5, and S97E at pH 5.6. Global fitting for all datasets yielded five exponentials. Similarly to the results at pH 7.4, the lifetimes include two fast components, ~0.3–0.7 μs and ~3–7 μs, and two slow components, ~3–70 ms and ~200–600 ms. The fifth component in the 60-μs to 2-ms region has smaller amplitudes except for the S97E mutant.

The spectral forms produced from the deconvolution of the sequential intermediates are shown in Fig. 9, and their time evolutions are displayed in Fig. 10. Only the WT at pH 8.5, Figs. 9 *B* and 10 *B*, shows significant levels of all four forms seen at pH 7.4. At low pH, the WT and S97E, Figs. 9 *A* and *D*, respectively, possess no M-like spectral form, whereas the D234N in Fig. 10 *C* shows it but at an extremely low level bordering the range of resolution. For the S97E mutant at low pH (Figs. 9 *D* and 10 *D*), the early L′-like spectral form is present in three intermediates, thus spanning a somewhat longer time interval than at pH 7.4.

The time evolutions of the spectral forms clearly show no M-like form at low pH but enhanced late deprotonation of the Schiff base at high pH. As at pH 7.4, the D234N and S97E low-conductance mutants display low levels of the K-like and high levels of the L-like spectral forms, which, together with the absence of the M-like form at low pH, question the validity of the published photocycle models.

CONCLUSIONS

SVD analysis suggested the presence of four spectral forms, whereas global exponential fit of the time-resolved absorption
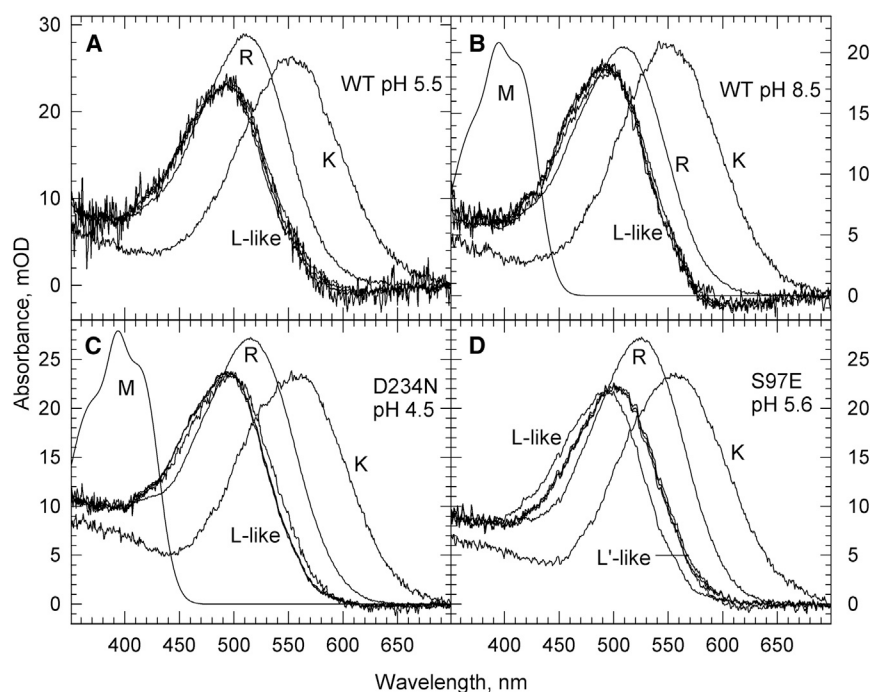

FIGURE 9 Spectral forms from the sequential intermediates. (*A*) WT pH 5.5, (*B*) WT pH 8.5, (*C*) D234N pH 4.5, and (*D*) S97E pH 5.6.
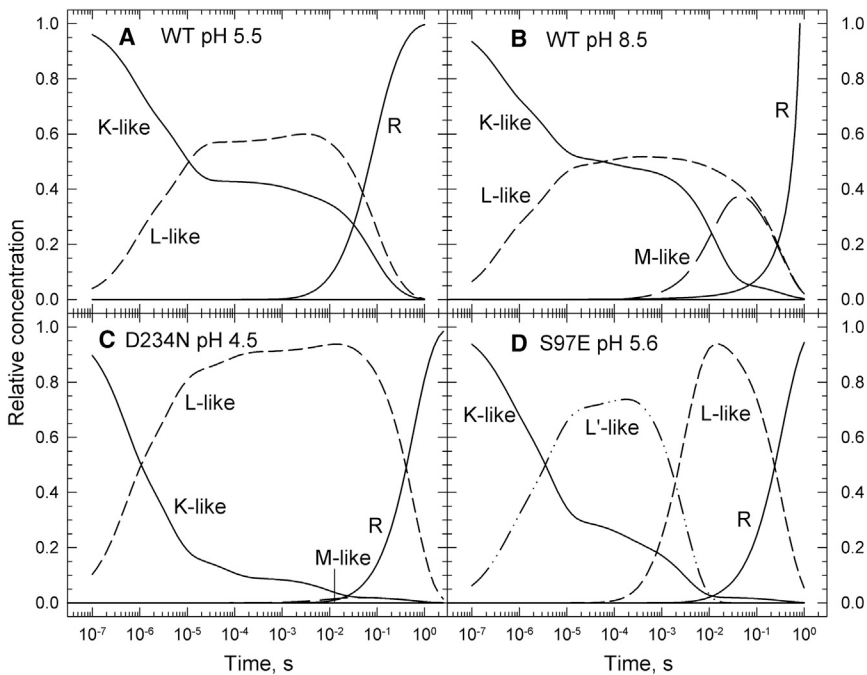
FIGURE 10 Time evolution of the absolute intermediate spectral forms. (*A*) WT pH 5.5, (*B*) WT pH 8.5, (*C*) D234N pH 4.5, and (*D*) S97E pH 5.6. A log timescale having 10 points per decade was used to produce the curves.

data of the WT *Gt*ACR1 and the D234N and A75E mutants produced five lifetimes, of which two are in the early-microsecond, two in the late-millisecond, and a fifth one of smaller amplitude in the millisecond time range. Deconvolution of sequential intermediate spectra confirmed the presence of four distinct spectral forms, K-like, L-like, M-like, and the recovered form, R. The S97E mutant also produced five lifetimes and, in addition to the four spectral forms mentioned, it showed an additional early L′-like spectral form less blue shifted than the common L-like form appearing at later times. Both red-absorbing (K-like) and blue-absorbing (L-like) species exist for the entire length of the photocycle. No transitions were detected in the time range of channel opening. In the time window of the open channel, WT *Gt*ACR1 and the A75E mutant showed nearly equal amounts of the K-like and L-like spectral forms. The mutants with low conductivity, D234N and S97E, displayed high levels of the L-like and low levels of the K-like spectral forms in the time window of open channel state.

Based on the results of the SVD analysis and spectral deconvolution and those of the global exponential fitting, we propose the existence of isospectral intermediates undergoing spectrally silent transitions in the photocycle of *Gt*ACR1 proteins. The longevity of the K-like and L-like spectral forms, and also the separation of the L-like form into early and late types in the S97E mutant, support this idea. The amplitude levels of the K-like and L-like spectral forms at times of open channel challenge the notion of assigning the L intermediate to the open channel state. Based on our data, the K-like spectral form is a more suitable candidate for that role. The absence of the M-like form in acidic environments raises questions about its

role in the photocycle. The evidence presented here points to the need for a complex mechanism for *Gt*ACR1 kinetics.

AUTHOR CONTRIBUTIONS

P.S., data collection, sample and manuscript preparation; I.S., experiment planning, data analysis, primary manuscript writer; E.C., data collection and manuscript preparation; H.L., sample preparation; J.L.S., experiment planning and manuscript preparation; D.S.K., experiment planning and manuscript preparation.

ACKNOWLEDGMENTS

DECLARATION OF INTERESTS

The authors declare no competing interests.

REFERENCES

1. Govorunova, E. G., O. A. Sineshchekov, …, J. L. Spudich. 2015. NEUROSCIENCE. Natural light-gated anion channels: A family of microbial rhodopsins for advanced optogenetics. *Science.* 349:647–650. https://doi.org/10.1126/science.aaa7484.

2. Mauss, A. S., C. Busch, and A. Borst. 2017. Optogenetic Neuronal Silencing in Drosophila during Visual Processing. *Sci. Rep.* 7, 13823. https://doi.org/10.1038/s41598-017-14076-7.

3. Messier, J. E., H. Chen, …, M. Xue. 2018. Targeting light-gated chloride channels to neuronal somatodendritic domain reduces their excitatory effect in the axon. *Elife.* 7, e38506. https://doi.org/10.7554/eLife.38506.

4. Mohammad, F., J. C. Stewart, …, A. Claridge-Chang. 2017. Optogenetic inhibition of behavior with anion channelrhodopsins. *Nat. Methods.* 14:271–274. https://doi.org/10.1038/nmeth.4148.

5. Mahn, M., M. Prigge, …, O. Yizhar. 2016. Biophysical constraints of optogenetic inhibition at presynaptic terminals. *Nat. Neurosci.* 19:554–556. https://doi.org/10.1038/nn.4266.

6. Li, H., C. Y. Huang, …, J. L. Spudich. 2019. Crystal structure of a natural light-gated anion channelrhodopsin. *Elife.* 8, e41741. https://doi.org/10.7554/eLife.41741.

7. Govorunova, E. G., Y. Gou, …, J. L. Spudich. 2022. Kalium channelrhodopsins are natural light-gated potassium channels that mediate optogenetic inhibition. *Nat. Neurosci.* 25:967–974. https://doi.org/10.1038/s41593-022-01094-6.

8. Stoeckenius, W., R. H. Lozier, and R. A. Bogomolni. 1979. Bacteriorhodopsin and the purple membrane of halobacteria. *Biochim. Biophys. Acta.* 505:215–278. https://doi.org/10.1016/0304-4173(79)90006-5.

9. Sineshchekov, O. A., H. Li, …, J. L. Spudich. 2016. Photochemical reaction cycle transitions during anion channelrhodopsin gating. *Proc. Natl. Acad. Sci. USA.* 113:E1993–E2000. https://doi.org/10.1073/pnas.1525269113.

10. Ernst, O. P., D. T. Lodowski, …, H. Kandori. 2014. Microbial and animal rhodopsins: structures, functions, and molecular mechanisms. *Chem. Rev.* 114:126–163. https://doi.org/10.1021/cr4003769.

11. Dreier, M. A., P. Althoff, …, K. Gerwert. 2021. Time-resolved spectroscopic and electrophysiological data reveal insights in the gating mechanism of anion channelrhodopsin. *Commun. Biol.* 4:578. https://doi.org/10.1038/s42003-021-02101-5.

12. Sineshchekov, O. A., E. G. Govorunova, …, J. L. Spudich. 2015. Gating mechanisms of a natural anion channelrhodopsin. *Proc. Natl. Acad. Sci. USA.* 112:14236–14241. https://doi.org/10.1073/pnas.1513602112.

13. Szundi, I., H. Li, …, D. S. Kliger. 2015. Platymonas subcordiformis Channelrhodopsin-2 Function: I. THE PHOTOCHEMICAL REACTION CYCLE. *J. Biol. Chem.* 290:16573–16584. https://doi.org/10.1074/jbc.M114.631614.

14. Szundi, I., S. G. Pitch, …, D. S. Kliger. 2021. Styrene-maleic acid copolymer effects on the function of the GPCR rhodopsin in lipid nanoparticles. *Biophys. J.* 120:4337–4348. https://doi.org/10.1016/j.bpj.2021.09.012.

15. Henry, E. R., and J. Hofrichter. 1992. Singular Value Decomposition - Application to Analysis of Experimental Data. *Methods Enzymol.* 210:129–192.

16. Szundi, I., J. W. Lewis, and D. S. Kliger. 1997. Deriving reaction mechanisms from kinetic spectroscopy. Application to late rhodopsin intermediates. *Biophys. J.* 73:688–702. https://doi.org/10.1016/S0006-3495(97)78103-7.

17. Sineshchekov, O. A., E. G. Govorunova, …, J. L. Spudich. 2019. Opposite Charge Movements Within the Photoactive Site Modulate Two-Step Channel Closing in GtACR1. *Biophys. J.* 117:2034–2040. https://doi.org/10.1016/j.bpj.2019.10.009, <Go to ISI>://WOS:000497815800023.

18. Kim, Y. S., H. E. Kato, …, K. Deisseroth. 2018. Crystal structure of the natural anion-conducting channelrhodopsin GtACR1. *Nature.* 561:343–348. https://doi.org/10.1038/s41586-018-0511-6.

19. Tsujimura, M., K. Kojima, …, H. Ishikita. 2021. Proton transfer pathway in anion channelrhodopsin-1. *Elife.* 10, e72264. https://doi.org/10.7554/eLife.72264.